Effect of Grid Topology on Numerical Simulations of Flow Fields around Wind Turbine Nacelle Anemometer

M. Tata[1,2†], A. Smaili[2] and C. Masson[3]

[1] *Centre de Développement des Energies Renouvelables. BP 62 Route de l'Observatoire, Bouzaréah, 16340, Algiers, Algeria*
[2] *Laboratoire de Génie Mécanique et Développement, Ecole Nationale Polytechnique ENP, BP 182 El-harrach, 16200, Algiers, Algeria*
[3] *Laboratoire de recherche sur l'aérodynamique des éoliennes en milieu nordique, Ecole de Technologie Supérieure ETS, 1100 Rue Notre-Dame Ouest, Montréal, QC H3C 1K3, Canada*

†*Corresponding Author Email: m.tata@cder.dz*

ABSTRACT

In this paper, the effect of mesh topology on the numerical predictions of the immediate near wake region of a horizontal axis wind turbine is investigated. The present work focuses on the nacelle anemometry measurements. Steady Reynolds Averaged Navier-Stokes (RANS) equations are applied to describe the airflow around the wind turbine nacelle. The k-ε turbulence model is used. To model the turbine rotor, the approach based on the actuator disc concept is considered. The computational domain has been meshed with five different configurations of grid; namely, quasi-structured, unstructured and three different hybrid grids constituted of blending of quasi-structured and unstructured grids. The obtained results are compared to the available experimental data. The hybrid mesh with quasi-structured grid in the boundary layer region and unstructured grid in the vicinity of the nacelle is found to be more promising to simulate the near wake generated downstream of the wind turbine nacelle and to predict accurately the nacelle anemometry measurements.

Keywords: Wind turbine; Nacelle anemometry; Turbulent flow; Numerical simulation; Navier-Stokes equations.

1. INTRODUCTION

Wind farm owners need to measure free stream wind speed (U_{inf}) to access wind turbine performances and monitor turbine production and safety. The setting of met mast ahead each wind turbine is an expensive investment. To save installation costs, a good alternative for meteorological masts is the setting of an anemometer on the wind turbine nacelle. However, nacelle anemometers measure the wind speed in the immediate near wake rotor that is different from the (U_{inf}). In order to deduce the (U_{inf}) from the Nacelle Wind Speed (U_n), a correlation is established between the (U_n) and the (U_{inf}) by using the nacelle anemometry technique. This technique is based upon the fact that a relationship between the (U_n) and the (U_{inf}) established for a reference turbine can be applied and generalized to other similar turbines (Antoniou *et al.*. (1997), Smaili and Masson (2004) and IEC 61400-12-2 (2013)).

Many authors have analyzed and developed nacelle anemometry correlations by using Computational Fluid Dynamics (CFD). In1997, Antouniou *et al.* (1997) investigated the advantages and limits of using nacelle anemometry as an alternative for tower measurement. They considered different parameters such as the nacelle anemometer positions, the blade pitch angle, the yaw angle, the rotor and eddies generated by blades root. The authors noticed that the wind speed measured at the met mast anemometer is close to the one of the nacelle anemometer for low wind speeds. Otherwise, for high wind speed (> 8 m/s), the difference is significant. The authors also investigated the effect of anemometer height on the nacelle. They noticed that the measured velocity decreases when the anemometer height increases because the anemometer moves-up to the high velocity deficit region. For parked wind turbines, the authors showed that U_n is 20% to 30% higher than U_{inf}. Smaili and Masson (2004) investigated the appropriate anemometer position on the wind turbine nacelle for two cases: rotor-on (operating mode) and rotor-off (standby mode). They noticed that the variation of U_n between both cases is 10%. This small difference is

due to the anemometer location in the cylindrical blade part area where there is no energy extraction from wind. Then, Masson and Smaili (2006) developed a numerical method for the simulation of the turbulent flow around the nacelle of a horizontal axis wind turbine. The authors assessed mainly the impact of the variation of the blade pitch angle and the atmospheric turbulence upon the relationship between U_n and U_{inf}. Later, El Kasmi *et al.* (2008) used actuator disk model combined with RANS equations to describe the wind turbine rotor. The authors considered the nacelle as disk permeable surface normal to the incoming flow, on which the drag coefficient is set to unity. They showed that the nacelle has an influence on the flow field in the near wake of the wind turbine rotor. Frandsen *et al.* (2009) also performed a numerical study on the nacelle anemometer. They adopted the actuator disk concept to model the wind turbine. Same as Smaili and Masson (2004), the authors noticed that the wind speed close to the nacelle was approximately equal to the free-wind speed. Afterwards, Ameur *et al.* (2011) studied the time-averaged turbulent flow around a horizontal axis wind turbine nacelle. They investigated the impact of the rotor-nacelle interaction and their influence on the U_n. Recently, Goh *et al.* (2016) developed U_{inf} correlations to vertical axis wind turbine, similarly to horizontal axis wind turbines; the authors studied Savonius wind turbine performances by measuring wind speed above the wind turbine. They established the relationship between that position and U_{inf} using CFD simulations and compared the obtained results to their experimental measurements. The authors noticed that wind speed at the anemometer position above the wind turbine is 9% higher than U_{inf}. The wind turbine power coefficient C_p calculated using U_{inf} shows an increase of 25% at 12m/s compared to C_p reported by other researchers who considered wind speed from the anemometer above the wind turbine.

Grid topologies are classified into structured and unstructured depending on the shape and connectivity of the grid elements. Structured grids are generally composed of quadrilaterals in two dimensions and hexahedral in three dimensions. Among Computational Fluid Dynamics (CFD) studies using structural grids, Maizi *et al.* (2017) studied the flow around a wind turbine blade using structured meshes.

Unstructured meshes have elements with irregular connectivity that is not predictable and must be explicitly declared. Unstructured meshes are most commonly made of triangles or quadrilaterals in two dimensions and of tetrahedral, pyramids and prisms in three dimensions. Unstructured grids are mostly used for complex geometries because of their flexibility in refinement and reduced time in generating the grid (Mavriplis (2000)).

The use of unstructured grids in computational fluid dynamics is widely considered in the last two decades. Nowadays, mixed or hybrid grids gain popularity because of the improved efficiency and accuracy for viscous flow simulations over pure tetrahedral grids. Tsoutsanis *et al.* (2014) studied

the flow around a sphere using hybrid grids. The boundary layer region was discretized by prisms (quasi-structured grids) and the rest of the domain by tetrahedral elements. Zhang *et al.* (2012) noticed that hybrid grids are more efficient than the fully unstructured tetrahedral grids especially for viscous flow simulations. However, as shown by Anderson (1994), the overall time to generate grids about complex configurations is much shorter for unstructured grids compared to structured grids. Lysenko *et al.* (2013) concluded that the influence of grid topology leads to a difference between results of 5%. In the same context, Cao *et al.* (2016) analyzed the flow past a square cylinder and emphasized the effect of meshing strategy on the numerical accuracy. They concluded that mesh refinement in the wake of the square cylinder could improve the prediction of the velocity distribution and overcome the earlier energy decay of turbulence caused by artificial dissipation.

In the present paper, the effect of mesh topology on the efficiency of numerical simulations of the flow near the wind turbine nacelle is investigated. The aim of this work is to reduce CPU time and to enhance numerical prediction accuracy of the nacelle anemometer correlation by determining a proper mesh topology. This study is applied to the NORDEX N80/2500 wind turbine. In the next section, the mathematical model describing the physical problem is presented. The numerical method adopted to solve the resulting governing equations is presented in the third section. Finally, the simulation results are discussed in section 4.

2. METHODOLOGY

2.1 Governing Equations

The flow around the wind turbine nacelle is described by the steady and incompressible Reynolds Averaged Navier-Stokes (RANS) equations and they are written as follows:

$$\frac{\partial u_i}{\partial x_i} = 0 \tag{1}$$

$$u_j \frac{\partial u_i}{\partial x_j} = -\frac{1}{\rho}\frac{\partial p}{\partial x_i} + \frac{\partial}{\partial x_j}\left[\frac{(\mu+\mu_t)}{\rho}\frac{\partial u_i}{\partial x_j}\right] + s \tag{2}$$

where, u_i is the time-averaged velocity component in the x_i direction, p the time-averaged pressure, ρ the fluid density, μ and μ_t are respectively molecular viscosity and turbulent viscosity and s is the source term.

2.2 Turbulence Modelling

For the closure of the above equations, several turbulence models were used in previous works such as the standard k-ε model, the k-ω model of Wilcox and the Menter k-ω SST model (Tata *et al.* (2014), Bouhelal *et al.* (2018)). It has been shown that the k-ε model is the more suitable model to our case. Then it is used in the present work. The equations of k and ε are written as follows:

$$\rho u_i \frac{\partial k}{\partial x_i} = \frac{\partial}{\partial x_i}\left(\left(\mu + \frac{\mu_t}{\sigma_k}\right)\frac{\partial k}{\partial x_i}\right) + P_k - \rho\varepsilon \quad (3)$$

$$\rho u_i \frac{\partial \varepsilon}{\partial x_i} = \frac{\partial}{\partial x_i}\left(\left(\mu + \frac{\mu_t}{\sigma_\varepsilon}\right)\frac{\partial \varepsilon}{\partial x_i}\right) + \frac{C_{\varepsilon 1}\varepsilon}{k}P_k$$
$$- \frac{\rho C_{\varepsilon 2}\varepsilon^2}{k} \quad (4)$$

where, P_k is the kinetic energy production.

$$P_k = -\mu_t\left(\frac{\partial u_i}{\partial x_j} + \frac{\partial u_j}{\partial x_i}\right)\frac{\partial u_i}{\partial x_j} \quad (5)$$

Turbulence model constants used are given in Table 1.

Table 1 Turbulence model constants (*Smaili and Masson* (2004), Masson *et al.* (2006))

C_μ	$C_{\varepsilon 1}$	$C_{\varepsilon 2}$	σ_k	σ_ε
0.0333	1.44	1.92	1	1.3

2.3 Rotor Modelling

The full Navier-Stokes method for the wind turbine rotor simulation is a complex and time-consuming approach. Several models for the numerical simulation of the wind turbine rotor are considered by many authors (Réthoré *et al.* (2014), Hansen (2000), Troldborg *et al.* (2011) and Dobrev *et al.* (2007)). The most used rotor model is the one based on the actuator disc approach (Troldborg *et al.* (2015) and Van der Laan *et al.* (2015)). The wind turbine rotor in the present study is thus modelled using the concept of the actuator disk (AD). The actuator disc theory consists to introduce a source term in the momentum equation, which represents the forces loading on the rotor (Masson *et al.* (2001)). The total uniform thrust T applied by the rotor into the fluid is given by Eq. (6) (see Fig. 1).

$$T = \frac{\rho(U_{\inf})^2}{2}\pi R^2 C_T \quad (6)$$

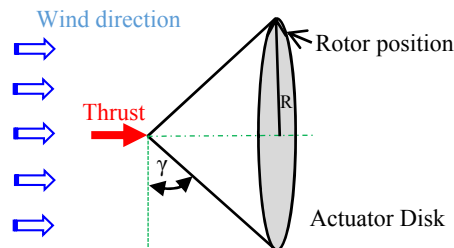C_T is the thrust coefficient and R is the rotor radius.

Fig. 1. Actuator Disc with uniform thrust.

γ: is the rotor conning angle (it is equal to zero in our case).

3. NUMERICAL RESOLUTION

3.1 Formulation

The OpenFoam 2.3.1 CFD solver, based on a collocated finite volume method, is used to solve the governing equations. A subprogram is written in OpenFOAM to model the actuator disc. This later is modelled as a total uniform thrust force and introduced as source term in the momentum equation.

The Semi-Implicit Method for Pressure-Linked Equations (SIMPLE) algorithm is used for the resolution of the coupled velocity/pressure equations. The diffusion term is discretized by a second order centered scheme (Gauss Linear Corrected) and the convection term is discretized by a second order scheme (Gauss linear).

3.2 Computational Domain and Boundary Conditions

The computational domain is a bi-dimensional H-type, where the wind turbine nacelle is considered as axis-symmetric (Fig. 2). The mast is neglected. In Fig. 2, x_up is the upstream distance from the inlet boundary to the wind turbine rotor, x_down is the distance from the wind turbine rotor to the outlet boundary and y_up is the distance from the wind turbine hub to the upper limit of the computation domain. Five grid configurations have been considered; namely, quasi-structured quadrilateral grids, unstructured triangular grids and three hybrid grids constituted from a blending of quasi-structured and unstructured grids. These different grid topologies are presented in details in Fig. 3.

The applied boundary conditions are: Inlet, Outlet, Wall and Symmetry.

Inlet condition is applied on the East and Top Boundaries (Fig. 2): Uniform velocity profile and k-ε values corresponding to the neutral planetary boundary layers properties at hub height are prescribed at the inlet boundary (Masson *et al.* (2006)). The turbulent kinetic energy k and the turbulent dissipation rate ε in the inlet boundary are defined as follows (Lin and Ebadian (1999)):

$$k = \frac{3}{2}(U_{\inf} \times I)^2 \quad (7)$$

and

$$\varepsilon = \frac{C_\mu^{3/4} \times k^{3/2}}{l} \quad (8)$$

where, I is the turbulent intensity that is set to 4% and l is the turbulent length scale $l = 0.07 \times L$; L is a reference length set to the wind turbine nacelle length ($L = 12$m).

Outlet condition is applied on the West boundary: The fluxes of all diffusive quantities in the direction normal to the outlet surface are assumed zero.

Wall no-slip condition is prescribed on the nacelle surface with a two-velocity scale wall-function:

Logarithmic zone (y+ > 11.225):

$$u^+ = \frac{1}{\kappa}\ln(E\,y^+) \quad (9)$$

and

$$y^+ = \frac{\rho C_\mu^{1/4} k_1^{1/2} y_1}{\mu} \quad (10)$$

Viscous Sub-Layer + Buffer Zones (y+< 11.225) :
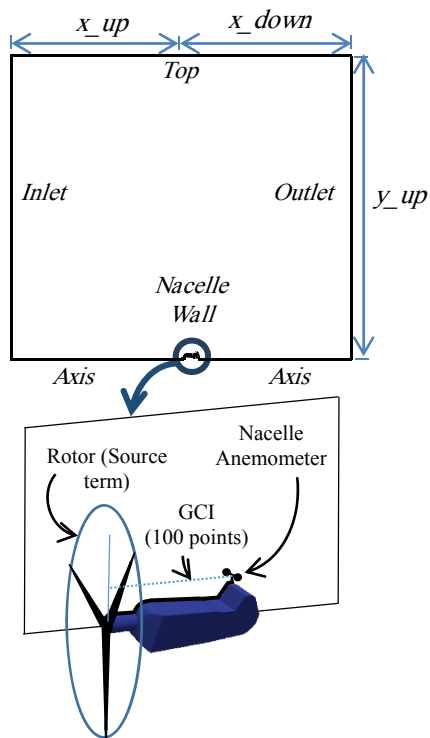
$$u^+ = y^+ \qquad\qquad (11)$$

Fig. 2. Computational domain and boundary conditions.

3.3 Grid Dependency Study

The aim goal in the present work is to assess the influence of the grid topology on the numerical predictions. For this purpose, five grid configurations are compared namely, quasi-structured quadrilateral grids (Pr), unstructured triangular grids (Tr), and three hybrid grids constituted from a blending of quasi-structured and unstructured grids which are; (H1, H2 and H3) (Fig. 3). The first hybrid mesh (H1) is a blending of quasi-structured prismatic grids in the boundary layer and in the vicinity of the wind turbine nacelle regions, and unstructured triangular in the rest of the computational domain. In the second hybrid mesh (H2), quasi-structured grids are built in the boundary layer region only; the rest of the domain is meshed with triangular cells. The boundary layer of the third hybrid grid (H3) is meshed with prisms, the near region of the wind turbine nacelle is meshed with triangular cells and the rest of the domain region is meshed with quasi-structured prismatic cells. Figure 3, (a), (b) and (c) represent respectively the mesh in the whole domain, mesh topology in the vicinity of the wind turbine nacelle and mesh topology in the boundary layer region. For all cases, the meshes are fine near the nacelle surface in order to predict more accurately the flow in the boundary layer and become coarser when going away from the nacelle wall to optimize the CPU time. The total number of cells varies between 9954 and 764857 cells, depending on the grid shape and size.

(i) Quasi-structured prismatic based grid Pr.

(ii) Unstructured triangular based grid Tr.

(iii) Hybrid grid (H1).

(iv) Hybrid grid (H2).
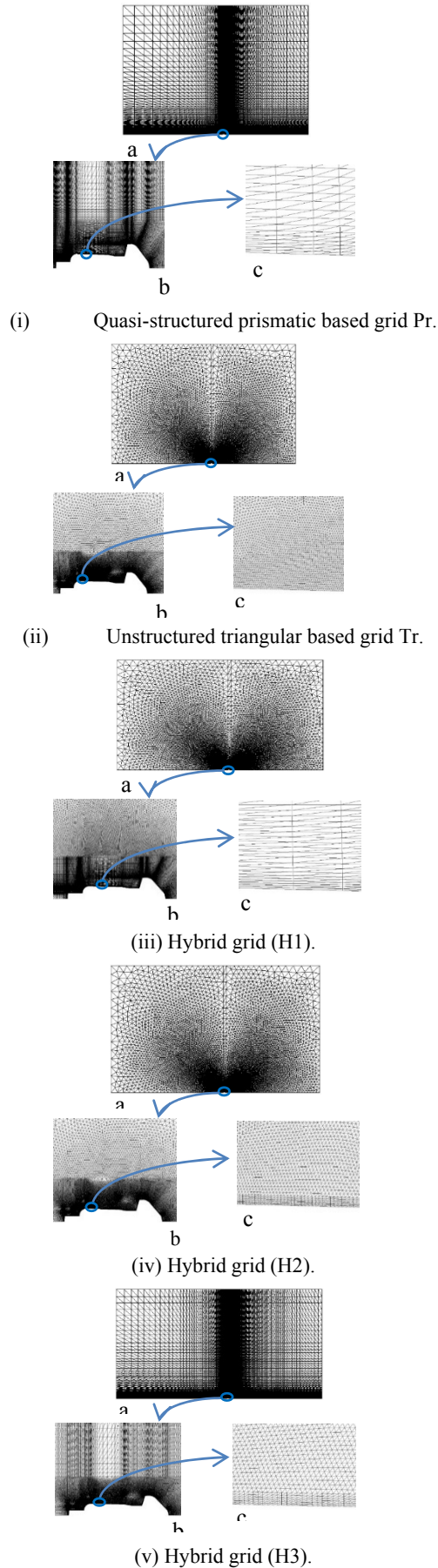

(v) Hybrid grid (H3).

Fig. 3. Mesh topologies.

The Grid Convergence Index (GCI) method based on Richardson extrapolation is applied to study the independence of the mesh on the solution. Many authors used the GCI method to study the grid dependency for their computations (Celik (1993); Roache *et al.* (1986); Eça *et al.* (2006) and Stern *et al.* (2006)). The following relations give GCI calculation:

$$GCI^{ij} = \frac{f \times e_{rms}^{ij}}{r_{ij}^{ap} - 1} \quad (12)$$

where:

$f = 3$, e_{rms}^{ij} is the root-mean-square of the relative errors, which is used to provide an initial measure of grid convergence for selected points. r_{ij} is the grid refinement ratio and ap is the apparent convergence order. GCI_{ij} indicates how far the solution from the asymptotic value is.

The root-mean-square of the relative errors is calculated as follows:

$$e_{rms}^{ij} = \left(\frac{\sum_{l=1}^{m} \left(e_a^{ij} \right)^2}{m} \right)^{1/2} \quad (13)$$

e_a^{ij} : is the relative error, which is given by:

$$e_a^{ij} = \left| \frac{\phi_j - \phi_i}{\phi_j} \right| \quad (14)$$

and m is the number of points considered for *GCI* calculations. The grid refinement ratio is given by:

$$r_{ij} = \left(\frac{n_i}{n_j} \right)^{(1/D)} \quad (15)$$

where, n refers to the number of nodes of the corresponding grid, $D = 2$ for bi-dimensional case and $D = 3$ for three-dimensional case. The recommended refinement ratio values are $r_{ij} > 1.3$ (Celik *et al.* (2008)).

The apparent convergence order is expressed as follows:

$$ap = \frac{1}{\ln(r_{ij})} \left| \ln \left| \theta_{(i+1, j+1)} / \theta_{ij} \right| + q \right| \quad (16)$$

with,

$$\begin{cases} q = \ln\left(\dfrac{r_{ij}^{ap} - 1}{r_{i+1, j+1}^{ap} - 1} \right) & if \left(\theta_{i+1, j+1} / \theta_{i,j} \right) > 0 \\[4mm] q = \ln\left(\dfrac{r_{ij}^{ap} + 1}{r_{i+1, j+1}^{ap} + 1} \right) & if \left(\theta_{i+1, j+1} / \theta_{i,j} \right) < 0 \end{cases}$$

where, $\theta_{i+1, j+1} = \phi_{i+1} - \phi_{j+1}$ and $\theta_{ij} = \phi_i - \phi_j$

ϕ is the variable of interest (nacelle anemometer velocity for our case) for different grid refinements.

The relative errors are determined for m consistent points located in the computational domain. Hefny *et al.* (2008) studied the flow around a building and selected 1000 points distributed around the building to perform their GCI calculations. For a two-dimensional turbulent backward-facing-step flow, Celik and Karatekin (1997) considered 22 points. In the present work, 100 points above the wind turbine nacelle are considered (Fig. 2).

4. RESULTS AND DISCUSSION

This study is applied to the Horizontal Axis Wind Turbine NORDEX N80/2500. Their experimental thrust coefficients are given in table 2. In the present work, the rotor coning angle γ is set to 0°. An anemometer is located on the nacelle at a distance of 9.3 m from the rotor hub center in the x direction and 3.2 m in the y direction (Ameur *et al.* (2011)). To validate the proposed numerical approach, actual results are compared to experimental data of ECN (Energy research Center of the Netherlands) (Eecen *et al.* (2007)).

First, a dependence study of the domain size is performed to determine the optimum computational domain size. Then the grid independence study is carried out using the GCI method. Afterwards, the simulations of the flow field around the wind turbine nacelle are performed, the results are discussed and the U_n versus U_{inf} correlation is established. Two wind rotor configurations are considered: "rotor on" and "rotor off". In "rotor on", the wind turbine is operating. In "rotor-off", the wind turbine is stopped. All simulations are carried out on a workstation HP Z820 with 24 processors used in parallel with MPI (Message Passing Interface) utility.

Table 2 Experimental Thrust coefficients versus free stream wind speed

U_{inf} (m/s)	5	10	15	20
C_{Texp}*	0.793	0.689	0.305	0.128

*Ameur *et al.* (2011)

4.1 Computational Domain

The effect of the computational domain size on the accuracy of the numerical predictions is investigated by varying the values of the parameters x_up, x_down and y_up (Fig. 2). These distances are varied from 5R to 22.5R (R is the wind turbine rotor radius). These simulations are performed for both 'rotor-on' and 'rotor-off' configurations and for U_{inf} = 20 m/s.

Figure 4 shows the effect of the domain size on the solution. The parameter of interest is the wind speed at the nacelle anemometer position, since it is the key parameter in this work. From Fig. 4a, one can notice that numerical simulations are independent from the computational domain size starting from

the following sizes: x_up > 17.5R, y_up > 17.5R and x_down > 15R. Figure 4b shows that similar results are obtained for the operating wind turbine, which leads to conclude that the wind turbine rotor does not affect the nacelle anemometer measurements, as this anemometer is closer to the nacelle then to the turbine rotor. Thus, the nacelle anemometer for the present case is only affected by the nacelle shape. The computational domain size adopted in the following study is thus: y_up = 20R, x_up = 17.5R and x_down = 15R.
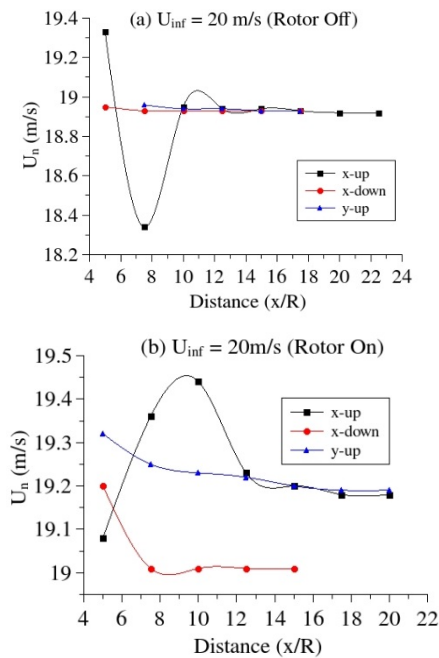

Fig. 4. Influence of computational domain size on the accuracy of numerical simulation.

4.2 Mesh Topology Effect

For each grid type, three mesh resolutions are considered: coarse, medium and fine. The cell geometry, grid resolution and Cells number for the five grid topologies are summarized in table 3. The GCI method is applied to the different mesh configurations. These simulations are performed for the case 'rotor on' with U_{inf} = 20m/s.

Figures 5 (a) and (b) show the axial velocity distributions above the wind-turbine nacelle for the quasi-structured grid Mesh 1 obtained for U_{inf} = 20 m/s.

These wind velocity distributions are extracted from the solution at a line located at the anemometer height i.e. at 3.2m from the rotor hub in the y direction. The extrapolated solution is the result corresponding to an infinitely small grid space.

The numerical uncertainties are represented by error bars in Fig. 5(b). These error bars are values of GCI at each point calculated by the average convergence order P_{avr}. The velocity distributions obtained for the other grid types show almost similar behavior therefore, they are not presented in this paper.

The root mean square of the relative error e_{rms} and the *GCI* based on velocity distribution near the wind turbine nacelle are given in Table 3. One can notice that the grid topology has an influence on both the grid resolution and the CPU time. The shortest CPU time is recorded for the grid *H2*. However, the lowest relative error is obtained with the hybrid grid *H3*. A high quality grid converged solution is typically assumed for e_{rms} values less than 1% (Hefny, (2008)). For the hybrid mesh *H3*, the values of e_{rms} and *GCI* are 1.5% and 3.4 % respectively. Thus, the hybrid grid *H3* corresponding to prismatic cells in the boundary layer region, triangular cells in the vicinity of the wind turbine nacelle and quasi-structured cells in the rest of the computational domain is selected in the present study.

Table 3 GCI calculations for the different grids

| Cell geometry	Grid resolution	Number of cells	r_{ij}	e_{rms} (%)	GCI (%)	CPU time (s)
Mesh 1 Prism *Pr*	Coarse	62118	1.5	5.5	9.1	5750 – 6187
	Medium	141372	1.7	1.6	1.7	6187 – 133772
	Fine	388340				
Mesh 2 Triangle *Tr*	Coarse	192265	1.3	5	3.3	8000 – 16316
	Medium	344556	1.5	2.5	3	16316 – 185410
	Fine	764857				
Mesh 3 Hybrid *H1*	Coarse	54893	1.8	15	3.9	150 – 2342
	Medium	186293	1.8	3.6	1.1	2342 – 66884
	Fine	579442				
Mesh 4 Hybrid *H2*	Coarse	91348	1.5	7.7	3.9	2304 – 21246
	Medium	198913	1.6	5.4	3.5	21246 – 65843
	Fine	524455				
Mesh 5 Hybrid *H3*	Coarse	92950	1.5	1.9	4.1	1203 – 23772
	Medium	204687	1.5	1.5	3.4	23772 – 87514
	Fine	455804				
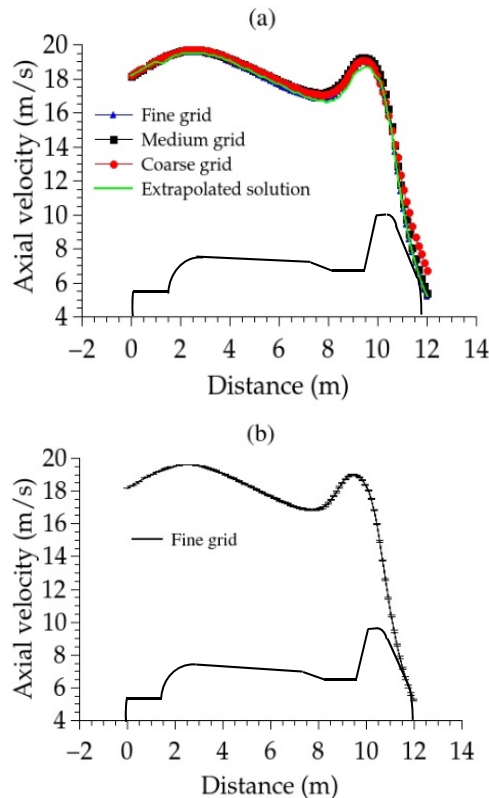
Fig. 5. Axial velocity distribution around the wind turbine nacelle for the quasi-structured prismatic based mesh P_r obtained at U_{inf} = 20 m/s.
a) Grid convergence. b) Fine-grid solution with error bar.

4.3   Flow Field Distributions Around the Wind Turbine Nacelle

Figure 6 shows pressure and axial velocity fields near the wind turbine nacelle for the rotor off case (standby mode). These simulations are performed for U_{inf} = 20m/s. In Fig. 6b, one can observe two zones with high flow speed where the velocity is about 130% the U_{inf}.

These speed-up regions are due to the curved shape of the nacelle near the rotor and the nacelle radiator near the anemometer. To get consistent measurements of the wind velocity, the nacelle anemometers should be located above the turbulent boundary layer to avoid the high velocity gradient generated by the nacelle wall and below the profiled-blade part to avoid the wind deficit generated by the rotor. Low wind speed zones, back flow and obstacles are not recommended positions for the nacelle anemometry.

The pressure and axial velocity fields near the wind turbine nacelle are depicted in Fig. 7 for the rotor-on case. These simulations are performed for U_{inf} = 20m/s. In Fig. 7b, as for the previous rotor-off mode, one can observe two high flow speed zones where the velocity is around 130% U_{inf}. Figure 7b shows that the nacelle anemometer is more affected by the wake generated by the nacelle rather than by the rotor wake. Figures 7c and 7d

show the wake and the flow deficit generated by the rotor with Actuator Disc modelling. The results obtained for other wind speeds exhibit similar behaviour. Thus, they are not presented in this paper.
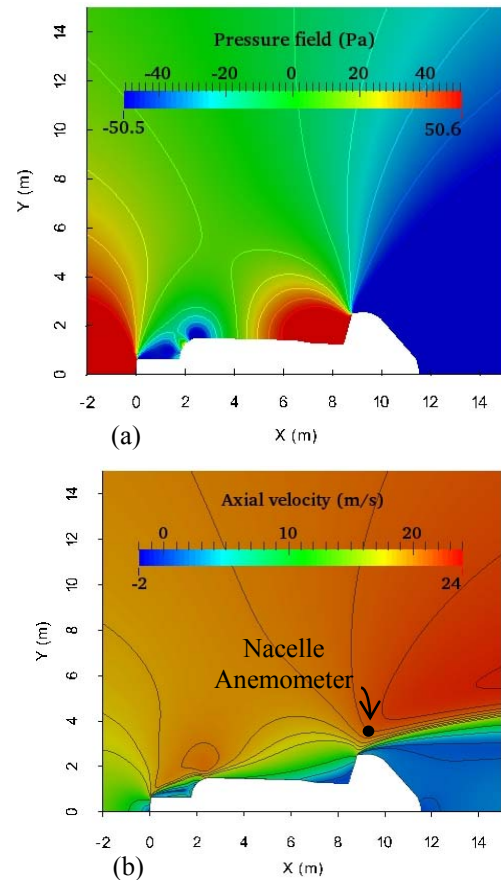

Fig. 6. Flow fields around the wind turbine nacelle (rotor off, U_{inf} = 20m/s)
a)-Pressure field. b)-Axial velocity field.

4.4   Nacelle Anemometry

Figure 8 shows the evolution of the axial wind velocity at the position of the nacelle anemometer for both rotor-off and rotor-on cases. These results are compared to the experimental data of Eecen *et al.* (2007). One can notice that the present results are in good agreement with the experimental data; an average shift up of 2% is found. The present results are also compared to those of Ameur *et al.* (2011). Figure 8 (a) shows that, for the rotor on mode, The U_n results are underestimated by about 8% in Ameur *et al.* (2011). This might be attributed to the computational domain size as they considered a smaller domain size. This difference could also be due to the mesh strategy adopted by the authors as they considered structured mesh for the entire computational domain. Indeed, the results obtained for the two grid topologies: H3 and Unstructured triangular grids Tr presented in Fig. 9a for rotor on case show that the greatest average relative error is recorded for the unstructured grid and is greater than 5%, which confirms the results found by Lysenko *et al.* (2013). The average relative error for the selected hybrid grid (H3) is around 2%.

(a)

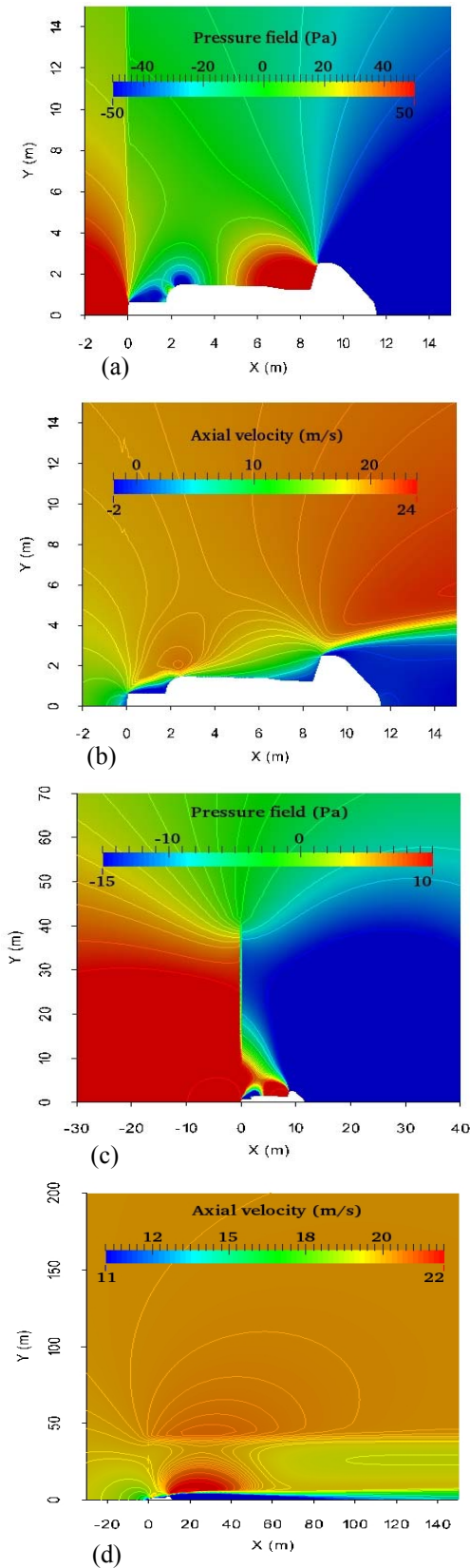(b)

(c)

(d)

Fig. 7. Flow fields around the wind turbine nacelle (rotor on, $U_{inf} = 20$m/s)
a)-Pressure field around the nacelle
b)-Axial velocity field around the nacelle
c)- Pressure field in the rotor wake.
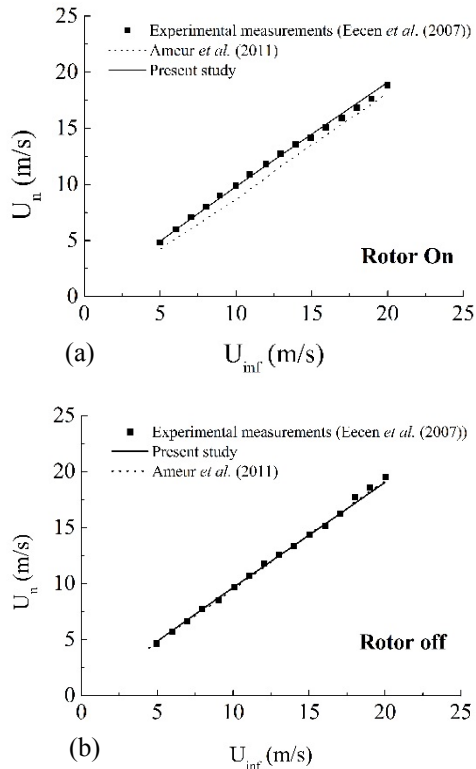**d)- Axial velocity field in the rotor wake.**

(a)

(b)

Fig. 8. Nacelle Wind Speed (at anemometer position) versus Free Stream Wind Speed.
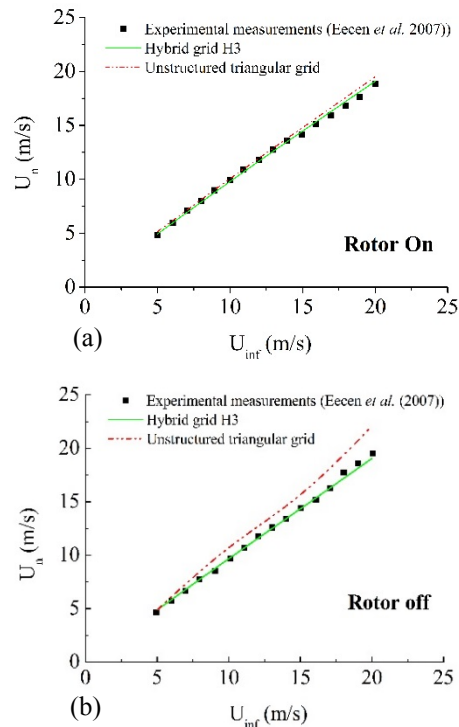

(a)

(b)

Fig. 9. Nacelle Wind Speed versus Free Stream Wind Speed obtained for different grid topologies.

3.   CONCLUDING REMARKS

In the present paper, the fluid flow in the vicinity of the horizontal axis wind turbine nacelle NORDEX

N80 has been numerically studied. The open source code OpenFOAM was used to solve the governing equations. First, the optimization of computational domain size was carried out. It was shown that the computational domain size is consistently dependent on nacelle shape rather than on the wind turbine rotor which does not affect the computational domain size dependency. For computational domain meshing, it was shown that the grid topology has appreciable effects on the grid resolution and CPU time. For hybrid mesh type *H3*, which combines quasi-structured mesh far from the nacelle and unstructured mesh in the vicinity of the nacelle, significant decreases of CPU time have been noticed. However, the grid topology does not have noticeable effect on the accuracy of flow field prediction in the immediate near wake of the wind turbine. The hybrid mesh style *H3*, is thus more adapted to predict the nacelle anemometry measurements and to simulate flow field in the near wake generated downstream of the wind turbine rotor. The near wall region is recommended to be meshed with structured or quasi-structured meshes to correctly predict the turbulent boundary layer and the high velocity gradient generated in this region. The actuator disc approach is able to predict the near rotor wake with acceptable accuracy. Wind velocity values calculated at the position of nacelle anemometer for both cases (rotor off and rotor on) are in good agreement with experimental measurements.

Future works will be put mainly on more detailed rotor modelling, such as, actuator surface and extending the work to a full Navier-Stokes simulations. Then, three-dimensional simulations of the wind turbine in unsteady state regime could be tackled. In order to assess the effect of neighboring wind turbine on nacelle anemometry, it is instructive to consider the nacelle anemometer in a wind farm. The effect of sandstorm on nacelle anemometry could also be considered for wind farms sited in Saharan climate.

REFERENCES

Ameur, K., C. Masson and P. J. Eecen (2011). 2D and 3D Numerical simulation of the wind–rotor nacelle interation in an atmospheric boundary layer, *Journal of Wind Engineering and Industial Aerodynamics.* 99, 833-844.

Anderson, W. K. (1994). A grid generation and flow method for the Euler equations on unstructured grids. *Journal of Computational Physics.* 110, 23-38.

Antoniou, I., and T. F. Pederson (1997). Nacelle Anemometry on a 1MW wind turbine: comparing the power performance results by use of nacelle or mast anemometer. *Riso National Laboratory*, Roskilde, Denmark.

Bouhelal A., A. Smaili, O. Guerri and C. Masson (2018) Numerical Investigation of Turbulent Flow around a Recent Horizontal Axis Wind Turbine Using Low and High Reynolds Models. *Journal of Applied Fluid* Mechanics 11(1), 151-164.

Cao Y., and T. Tamura (2016). Large Eddy Simulations of flow past a square cylinder using structured and unstructured grids. *Computers and Fluids* 137, 36-54.

Celik, I. B., U. Ghia, P. J. Roache, C. J. Freitas, H. Coleman and P. E. Raad (2008). Procedure for estimation and reporting of uncertainty due to discretization in CFD applications. *Journal of Fluids Engineering* 130(7), 0780011.

Celik, I. and O. Karatekin (1997). Numerical Experiments on Application of Richardson Extrapolation with Non-uniform Grids. *Journal of Fluid Engineering* 119, 584-590.

Celik, I. (1993). Numerical uncertainty in fluid flow calculations: needs for future research. *ASME Journal of Fluids Engineering* 115, 194-195.

Dobrev, I., F. Massouh, M. Rapin. (2007) Actuator surface hybrid model. The Science of Making Torque from Wind: *Journal of Physics: Conference Series* 75, 012019.

Eça, L. and M. Hoekstra (2006). On the influence of the iterative error in the numerical uncertainty of ship viscous flow calculations. *26th Symposium on Naval Hydrodynamics*, Rome, Italy.

Eecen, P. J. and J. P. Verhoef (2007). EWTW Meteorological Database Description June 2003 – May 2007. ECN-E 07-041, *ECN Wind Energy*, Netherlands.

El Kasmi, A. and C. Masson (2008). An extended k–ε model for turbulent flow through horizontal axis wind turbines. *Journal of Wind Engineering and Industrial Aerodynamics* 96, 103-122.

Frandsen, S., J. N. Sørensen, R. Mikkelsen, T. F. Pedersen, I. Antoniou and K. Hansen (2009). The generics of wind turbine nacelle anemometry. *Europe's Premier Wind Energy Event.*

Goh, S. C., S. R. Boopathy and C. Krishnaswani (2016). Tow testing of Savonius wind turbine above a bluff body complemented by CFD simulation. *Renewable Energy.* 87, 332-345.

Hansen, M. O. l. (2000) *Aerodynamics of Wind Turbines.* James & James (Science Publishers) Ltd: London, UK.

Hefny, M. M., and R. Ooka (2008). Influence of cell geometry and mesh resolution on large eddy simulation predictions of flow around a single building. *Building Simulations* 1, 251-260.

IEC 61400-12-2, Wind turbines - Part 12-2: Power performance of electricity-producing wind turbines based on nacelle anemometry, (2013).

Laan, Van der, P. M., N. N. Sørensen, P-E. Réthoré, J. Mann, M. C. Kelly and N. Troldborg. (2015) The k-fp model applied to double wind turbine wakes using different actuator disk force methods. *Wind Energy* 18, 2223-2240.

Lin, C. X. and M. A. Ebadian (1999). The effects of

inlet turbulence on the development of fluid flow and heat transfer in a helically coiled pipe. *International Journal of Heat and Mass Transfer* 42 (4), 739-751.

Lysenko, D. A., I. S. Ertesvag and K. E. Rian (2013). Modeling of turbulent separated flows using OpenFOAM. *Computers and Fluids.* 80, 408-422.

Maizi, M., R. Dizene and M. C. Mihoubi (2017). Reducing Noise Generated from a Wind Turbine Blade by Pitch Angle Control using CFD and Acoustic Analogy. *Journal of Applied Fluid Mechanics* 10(4), 1201-1209.

Masson, C., A. Smaili (2006). Numerical study of turbulent flow around a wind turbine nacelle. *Wind Energy* 9, 281-298.

Masson, C., A. Smaili, and C. Leclerc (2001). Aerodynamic analysis of HAWTs operating in unsteady conditions. *Wind Energy* 4, 1-22.

Mavriplis, F. (2000). CFD in aerospace in the new millennium. *Canadian Aeronautics and Space Journal* 46(4) 167-179.

Réthoré P., P. V. D. laan, N. Troldborg, F. Zahle and N. N. Sørensen. (2014) verification and validation of an actuator disc model. *Wind Energy* 17, 919-937.

Roache, P. J., K. N. Ghia and F. M. White (1986). Editorial policy statement in the control of numerical accuracy. *ASME Journal of Fluids Engineering* 108, 2.

Smaili, A. and C. Masson (2004). On the rotor effects upon nacelle anemometry for wind turbines. *Wind Engineering.* 28(6), 695-714.

Stern, F., R. Wilson and J. Shao (2006). Quantitative V&V of CFD simulations and certification of CFD codes. *International Journal of Numerical Methods in Fluids* 50, 1335-1355.

Tata, M. and A. Smaili (August 2014). Effect of Turbulence Models on Nacelle Anemometry Numerical Simulations of the Horizontal Axis Wind Turbine NORDEX_N80. *13th International Conference on Sustainable Energy technologies* (SET2014). Geneva.

Troldborg, N., F. Zahle, P. E. Réthoré and N. N. Sørensen. (2015) Comparison of wind turbine wake properties in non-sheared inflow predicted by different computational fluid dynamics rotor models. *Wind Energy* 18, 1239-1250.

Troldborg N., C. Gunner, H. A. Larsen, K. S. Madsen, J. N. Hansen, N. Sørensen and R. Mikkelsen. (2011) Numerical simulations of wake interaction between two wind turbines at various inflow conditions. *Wind Energy* 14, 859-876.

Tsoutsanis, P., A. F. Antoniadis and D. Drikakis (2014). WENO schemes on arbitrary unstructured meshes for laminar transitional and turbulent flows. *Journal of Computational Physics* 256, 254-276.

Zhang, L., X. Chang, X. Duan, Z. Zhao and X. He (2012). Applications of dynamic hybrid grid method for three-dimensional moving/ deforming boundary problems. *Computers and Fluids* 62, 45-63.